PHYSICAL REVIEW A, VOLUME 62, 053404

Complete measurements of two-photon ionization of atomic rubidium using elliptically polarized light

Zheng-Min Wang[1,2] and D. S. Elliott[2]
[1]*Department of Physics, Purdue University, West Lafayette, Indiana 47907*
[2]*School of Electrical and Computer Engineering, Purdue University, West Lafayette, Indiana 47907*

(Received 28 April 2000; published 12 October 2000)

We report in detail our complete characterization of atomic photoionization via a single measurement, namely, that of the two-photon photoelectron angular distribution using elliptically polarized light. Through these measurements we are able to determine the atomic parameters necessary to unambiguously describe two-photon ionization of atomic rubidium. These parameters include relative cross sections for photoionization into various outgoing channels as well as the phase difference between the continuum S and D partial waves. We present a derivation of the angular distribution with arbitrarily polarized light in terms of these cross sections and phases, demonstrate the advantages of using elliptically polarized light, discuss details of the experiment, and report the results of our measurements in this paper. While measured phase differences are in excellent agreement with expected values over the entire range of photoelectron kinetic energy of our measurements from 0 to 0.5 eV, ratios of cross sections for photoionization into the two D channels are anomalous, suggesting unexpected fine structure effects in these continua.

PACS number(s): 32.80.Rm, 32.10.−f

I. INTRODUCTION

Various techniques for ''complete'' measurements of photoionization processes have been reported in the past [1–5]. A complete measurement is one in which all the relative photoionization cross sections for exciting the different outgoing waves, as well as the phase differences between these channels, are unambiguously determined. Most complete determinations have included a measurement of the photoelectron angular distribution for linearly polarized light, augmented by some other experimental or theoretical data. The latter is necessary since the former is insufficient to completely characterize the interaction. For example, Duncanson *et al.* [1] measured photoelectron angular distributions for two-color, two-photon ionization of atomic sodium. While both laser fields were linearly polarized for these measurements, the investigators varied the angle between the directions of the polarizations, and thus were able to extract relative cross sections and the continuum phase difference. Similar measurements were carried out in neon by Siegel *et al.* [2]. Simultaneous measurements of the angular distribution and the spin polarization of the photoelectrons were carried out by Kaminski *et al.* [3] in cesium, and in xenon by Heinzmann [4]. These spin polarization measurements involved Mott scattering detectors, adding significantly to the difficulty of the measurements. Hausmann *et al.* [5] studied inner shell ionization of magnesium through simultaneous measurements of the photoelectron angular distribution and the residual alignment of the ion. Observations of circular dichroism in photoelectron angular distribution measurements have also been identified for their potential in yielding phase differences and relative cross sections [6,7]. In these two-color, two-photon measurements the intermediate state is aligned by excitation with linearly polarized light in the first step, and the difference in the photoelectron angular distributions for left- and right-circularly-polarized beams inducing the second step of the ionization process is measured. In addition to the requirement of multiple measurements in each of these experiments, they typically yield only the cosine of the phase difference of continuum waves, rather than the phase difference directly. Since the cosine function is bivalued in the range $0–2\pi$, this ambiguity must be resolved by some other means.

Our present measurements are motivated largely through questions raised in previous incomplete two-photon ionization measurements carried out by our group [8]. These measurements consisted only of the photoelectron angular distribution for linearly polarized light, and so required additional measurements or theoretical results to draw any firm conclusions. Lacking either of these at the specific wavelengths used for our measurements, we presented analyses based on two different, equally reasonable assumptions, i.e., (1) that the continuum phases of the S and D channels are given accurately by the semiempirical quantum defect theory [9,10], or (2) that the magnitudes of the two-photon radial transition moments to the $\varepsilon d\,^2D_{3/2}$ and the $\varepsilon d\,^2D_{5/2}$ continuum channels are equal. In support of the first assumption, quantum defect phases have been shown to be in good agreement with the results of more rigorous theories in many systems. Conversely, bound state intensity ratios for the D series in rubidium [11] support the second assumption. Nonetheless, our earlier results showed that at most one of these assumptions could be true. When we extrapolated quantum defects measured from the bound state spectra [12–14] to the continuum, we were led to the conclusion that the relative cross sections for ionization into the continuum $^2D_{5/2}$ and $^2D_{3/2}$ channels were highly imbalanced. The second assumption left us with continuum channel phase differences that were in strong disagreement with expected values. We sought a measurement that would resolve the conflict.

1050-2947/2000/62(5)/053404(14)/$15.00

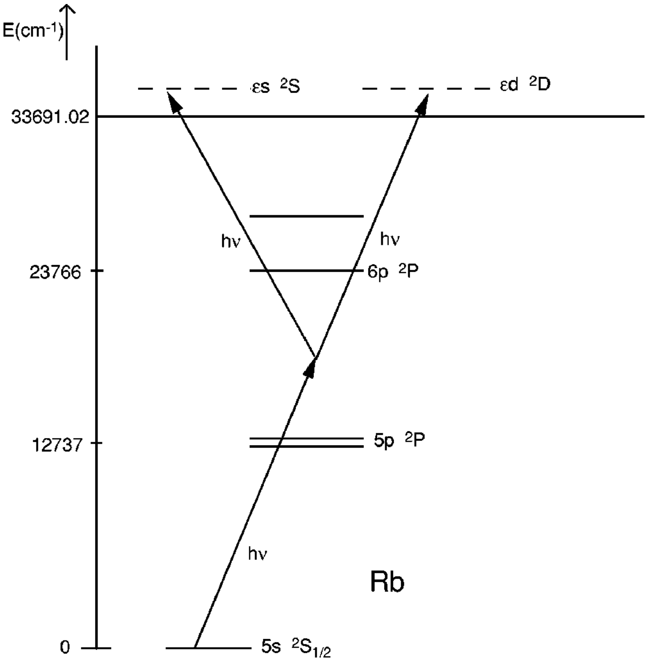

FIG. 1. Energy level diagram of atomic rubidium. The arrows indicate the transition pathways for nonresonant two-photon ionization.

We recently reported [15] measurements of photoelectron angular distributions for two-photon ionization of atomic rubidium using elliptically polarized light. These measurements represent a complete determination of the relative photoionization cross sections and continuum function phase differences through a single laboratory observation, in contrast to all previous methods discussed above. Our measurements yielded not only the magnitude of the phase differences (modulus π) but the sign as well. These phases are in excellent agreement with expected values over the entire range of photoelectron kinetic energies of our measurements from 0 to 0.5 eV. The cross sections to the D_J channels, however, showed a clear asymmetry, in approximate agreement with one of the possible conclusions of Ref. [8]. In this report we expand upon our results and discussion of Ref. [15]. We first present, in Sec. II, a theoretical derivation of the photoelectron angular distribution for two-photon ionization with arbitrarily polarized light, and then describe our apparatus for collecting the photoelectrons (Sec. III). Finally we present our measurements (Sec. IV) and our analysis of the results (Sec. V). We include a discussion of our technique for interpreting the image created by the photoelectrons in the Appendix.

II. THEORY

Two-photon ionization of an unaligned alkali metal atom initially in a ground $ns\ ^2S_{1/2}$ state produces an outgoing photoelectron in the continuum $\varepsilon s\ ^2S_{1/2}$, $\varepsilon d\ ^2D_{3/2}$, and $\varepsilon d\ ^2D_{5/2}$ states. See Fig. 1 for an energy level diagram of rubidium. The angular distribution of the photoelectrons ejected from this atom depends upon the relative magnitudes and phases of the three outgoing waves corresponding to each of these continuum channels. In this section we will present our derivation of the photoelectron angular distribution resulting from the two-photon interaction of rubidium with arbitrarily polarized light. We model this derivation after that of Bebb and Gold [16], who determined a general formulation for the differential cross section for multiphoton ionization, and Lambropoulos and Teague [17], who considered the two- and three-photon ionization of alkali metals driven by circularly or linearly polarized light.

In order to allow us to consider any polarization of the electric field, including linear, elliptical, and circular, we write the field as a plane wave of the form

$$\vec{E}(\vec{r},t)=E_0\hat{\epsilon}\exp[-i(\omega t-\beta y)]+\text{c.c.},\tag{1}$$

where $+\hat{y}$ defines the direction of propagation of the wave and $\hat{\epsilon}=\epsilon_1\hat{x}+\epsilon_3\hat{z}$ is a unit vector that describes the polarization of the field. We assign the vertical direction in our experiment as the $\hat{z}$ axis. The components $\epsilon_1=\epsilon_1'+i\epsilon_1''$ and $\epsilon_3=\epsilon_3'+i\epsilon_3''$ are in general complex, and the relative magnitude and phase difference between these components specify the polarization state of the light unambiguously. One polarization state of special interest in the present work is $\hat{\epsilon}=i\epsilon_1''\hat{x}+\epsilon_3'\hat{z}$, where ϵ_1'' and ϵ_3' are real and positive, and $\epsilon_1''\neq\epsilon_3'$. This vector describes left-elliptically polarized light, where we conform with the convention of Born and Wolf [18] for labeling the sense of rotation. In this state the $\hat{z}$ component leads the $\hat{x}$ component, and the electric field vector rotates counterclockwise as a function of time as viewed by an observer facing the laser source. The major axis of the ellipse is vertical for $\epsilon_3'>\epsilon_1''$ and horizontal for $\epsilon_3'<\epsilon_1''$. By parallel arguments, the vector $\hat{\epsilon}=-i\epsilon_1''\hat{x}+\epsilon_3'\hat{z}$ describes right-elliptically polarized light, which rotates clockwise when viewed by the same observer.

Bebb and Gold [16] presented a perturbative treatment of multiphoton ionization, in which they showed that the photoelectron angular distribution for two-photon ionization can be expressed in the form

$$\frac{d\sigma}{d\Omega}=\frac{m\alpha^2\omega^2|\vec{k}|}{\hbar}|T_{fg}|^2,\tag{2}$$

where m is the electron mass, $\alpha=e^2/\hbar c\approx 1/137$ is the fine structure constant, $\vec{k}$ is the momentum vector of the photoelectron, and

$$T_{fg}=\sum_n\frac{\langle\vec{k}|\hat{\epsilon}\cdot\vec{r}|n\rangle\langle n|\hat{\epsilon}\cdot\vec{r}|g\rangle}{(\omega_n-\omega_g-\omega)}\tag{3}$$

is the two-photon transition moment. In this expression, $\langle i|\hat{\epsilon}\cdot\vec{r}|j\rangle$ are the matrix elements of the projection of the electronic position operator onto the field polarization vector, while $\hbar\omega_n$ and $\hbar\omega_g$ are the atomic energies of the nonresonant intermediate states $|n\rangle$ and the initial state $|g\rangle$. In Fig. 1, all state energies are expressed relative to the ground state energy, so $\omega_g=0$. The summation is taken over all intermediate states that are dipole connected to the initial state, extending over the entire manifold of P states $|n\rangle = |np\,{}^2P_j, m_j\rangle$, where j is $\frac{1}{2}$ or $\frac{3}{2}$. Near resonance of the laser frequency with any of the intermediate states could lead to strong enhancement of the transition rate, but might also modify the angular distribution through effects related to the fine or hyperfine structure of the intermediate state [1,19–21]. We avoid these effects by using laser frequencies in the range from 16 950 cm^{-1} to 18 800 cm^{-1}. This single photon energy lies roughly halfway between the excitation energies of the $5p\,{}^2P_J$ and the $6p\,{}^2P_J$ intermediate states, as shown in Fig. 1.

Since the rubidium is initially unaligned, the two magnetic sublevels $m_s = \pm\frac{1}{2}$ of the ground state $|g\rangle = |5s\,{}^2S_{1/2}, m_s\rangle$ are equally populated. The angular distribution in Eq. (2) is thus determined by averaging over the initial spin states of $|g\rangle$, and summing over the final spin states of the continuum electron. The final state of photoelectron momentum $\vec{k}$ can be written as a linear superposition of angular momentum states [17,21]

$$|\vec{k}\rangle = \sum_{l'=0}^{\infty} \sum_{m_l'=-l'}^{l'} 4\pi(i)^{l'} e^{-i\xi_{l'}} G_{l'}(r) \times Y^*_{l'm_l'}(\Theta,\Phi) Y_{l'm_l'}(\theta,\phi)\chi_S . \tag{4}$$

The functions Y_{lm} are the spherical harmonics, the angular coordinates Θ and Φ represent the direction of the momentum of the photoelectron, while r, θ, and ϕ indicate the magnitude and direction of the electronic spatial position. The final orbital angular momentum states accessed by a two-photon process include $l' = 0,2$, i.e., $|f\rangle = |\varepsilon s\,{}^2S_{1/2}, m_j'\rangle$ or $|\varepsilon d\,{}^2D_{j'}, m_j'\rangle, j' = \frac{3}{2}, \frac{5}{2}$. The function χ_S represents the spin state of the photoelectron, whose projection along the $\hat{z}$ axis can be $\pm\hbar/2$. $G_{l'}(r)$ is the radial part of the continuum wave function, which approaches $(|\vec{k}|r)^{-1}\sin[|\vec{k}|r + |\vec{k}|^{-1}\ln(2|\vec{k}|r) - l'\pi/2 + \xi_{l'}]$ for $|\vec{k}|r \gg 1$. The asymptotic phase $\xi_{l'}$ of the continuum wave function can be written as the sum of two terms, the quantum-defect phase $\delta_{l'}$ and the Coulomb phase $\eta_{l'}$ [9,10]. The quantum-defect phase $\delta_{l'}$ is a slowly varying function of the kinetic energy ε of the photoelectron, and can be extrapolated from measurements [12–14] of the energies of the S and D bound states. For the S wave and D wave of rubidium this phase difference is given by

$$\delta_s - \delta_d = (1.7842 - 0.774\varepsilon + 1.75\varepsilon^2)\pi, \tag{5}$$

where ε is expressed in rydbergs. While the quantum-defect phase could in principal differ for the ${}^2D_{3/2}$ and ${}^2D_{5/2}$ channels, we estimate, using bound state energy levels [12], that the magnitude of this phase difference is only 0.003π. As we show later in this report, this estimated phase difference is smaller than the uncertainty in our measurements of $\xi_s - \xi_d$, and we therefore neglect any phase difference between the two continuum D channels. The Coulomb phase is of the form $\eta_{l'} = \arg\{\Gamma[l' + 1 - (i/\sqrt{\varepsilon})]\}$, where Γ is the complex gamma function. This leads to a Coulomb phase difference between the S and D waves of the form

$$\eta_s - \eta_d = \arctan\frac{1}{2\sqrt{\varepsilon}} + \arctan\frac{1}{\sqrt{\varepsilon}}. \tag{6}$$

The phase difference given by the sum of Eqs. (5) and (6) plays a strong role in the photoelectron angular distribution, and through our measurements we are able to determine this atomic parameter with very good precision, as we shall see later in this paper.

For arbitrary field polarization, the angular distribution becomes

$$\frac{d\sigma}{d\Omega} = \frac{m\alpha^2\omega^2|\vec{k}|}{2\hbar} \times \sum_g \left| \sum_{f,n} \frac{\langle\vec{k}|f\rangle\langle f|(\epsilon_1 x + \epsilon_3 z)|n\rangle\langle n|(\epsilon_1 x + \epsilon_3 z)|g\rangle}{\omega_n - \omega} \right|^2 . \tag{7}$$

We should expect that all m_j levels of the intermediate $np\,{}^2P_j$ states contribute, even in the absence of any spin-flip (fine structure) interactions, as the $\hat{z}$ component of the field can induce $\Delta m_l = 0$ transitions in each step of the interaction, and the $\hat{x}$ component drives $\Delta m_l = \pm 1$ transitions. After the absorption of two photons, the laser field excites a coherent superposition wave consisting of the $m_l' = 0$, ± 1, and ± 2 components of the $l' = 2$ state and the $l' = 0, m_l' = 0$ state. The proportions of this admixture state depend critically on the relative magnitude and phase of the field polarization components ϵ_1 and ϵ_3.

After evaluation of the matrix elements of Eq. (7), the differential cross section reduces to

$$\frac{d\sigma}{d\Omega} = \frac{m\alpha^2\omega^2|\vec{k}|}{2\hbar} \sum_{i,j=+/-} |T_{ij}^{(33)}\epsilon_3^2 + T_{ij}^{(13)}\epsilon_1\epsilon_3 + T_{ij}^{(11)}\epsilon_1^2|^2, \tag{8}$$

where $T_{ij}^{(pq)}$ are the spatial components of the two-photon transition moments. The indices $i,j = +$ or $-$ of the moments $T_{ij}^{(pq)}$ represent the spins of the ground and final state electrons, respectively, and $p,q = 1$ or 3 represent the relevant spatial components. The explicit forms of these moments are

$$T_{++}^{(33)} = \frac{1}{3} e^{i\xi_s} Y_{00}(\Theta,\Phi) S_{\bar{s}} - \frac{2}{3\sqrt{5}} e^{i\xi_d} Y_{20}(\Theta,\Phi) S_{\bar{d}}, \tag{9a}$$

$$T_{++}^{(13)} = \frac{1}{\sqrt{30}} e^{i\xi_d} \{2[Y_{21}(\Theta,\Phi) - Y_{2-1}(\Theta,\Phi)] S_{\bar{d}} - [Y_{21}(\Theta,\Phi) + Y_{2-1}(\Theta,\Phi)] S_{\Delta d}\}, \tag{9b}$$

TABLE I. Excitation pathways for the five radial transition elements.

Element	$\lvert g\rangle$	$\lvert n'p\,{}^2P_{j'}\rangle$	$\lvert f\rangle$
S_1	$\lvert 5s\,{}^2S_{1/2}\rangle$	$\lvert np\,{}^2P_{1/2}\rangle$	$\lvert \varepsilon s\,{}^2S_{1/2}\rangle$
S_2	$\lvert 5s\,{}^2S_{1/2}\rangle$	$\lvert np\,{}^2P_{3/2}\rangle$	$\lvert \varepsilon s\,{}^2S_{1/2}\rangle$
S_3	$\lvert 5s\,{}^2S_{1/2}\rangle$	$\lvert np\,{}^2P_{1/2}\rangle$	$\lvert \varepsilon d\,{}^2D_{3/2}\rangle$
S_4	$\lvert 5s\,{}^2S_{1/2}\rangle$	$\lvert np\,{}^2P_{3/2}\rangle$	$\lvert \varepsilon d\,{}^2D_{3/2}\rangle$
S_5	$\lvert 5s\,{}^2S_{1/2}\rangle$	$\lvert np\,{}^2P_{3/2}\rangle$	$\lvert \varepsilon d\,{}^2D_{5/2}\rangle$

$$T_{++}^{(11)}=\frac{1}{3}e^{i\xi_s}Y_{00}(\Theta,\Phi)\bar{S}_s+e^{i\xi_d}\Bigg\{\frac{1}{3\sqrt{5}}Y_{20}(\Theta,\Phi)\bar{S}_d$$

$$-\frac{1}{\sqrt{30}}\{[Y_{22}(\Theta,\Phi)+Y_{2-2}(\Theta,\Phi)]\bar{S}_d$$

$$-[Y_{22}(\Theta,\Phi)-Y_{2-2}(\Theta,\Phi)]S_{\Delta d}\}\Bigg\}, \tag{9c}$$

$$T_{+-}^{(33)}=\sqrt{\frac{2}{15}}e^{i\xi_d}Y_{21}(\Theta,\Phi)S_{\Delta d}, \tag{9d}$$

$$T_{+-}^{(13)}=\frac{1}{\sqrt{5}}e^{i\xi_d}\left[Y_{20}(\Theta,\Phi)-\sqrt{\frac{2}{3}}Y_{22}(\Theta,\Phi)\right]S_{\Delta d}, \tag{9e}$$

$$T_{+-}^{(11)}=-\frac{1}{\sqrt{30}}e^{i\xi_d}[Y_{21}(\Theta,\Phi)-Y_{2-1}(\Theta,\Phi)]S_{\Delta d}. \tag{9f}$$

The $--(-+)$ component is obtained from the $++(+-)$ component by changing $Y_{lm}\rightarrow Y_{l-m}$ and by changing the sign of the (13) component. The reduced two-photon transition moments S_r represent the average transition moment for excitation of the S continuum, $\bar{S}_s=(S_1+2S_2)/3$; the average transition moment for excitation of the D continuum, $\bar{S}_d=(5S_3+S_4+9S_5)/15$; and the asymmetry between the transition moments for the $D_{3/2}$ and $D_{5/2}$ waves, $S_{\Delta d}=(5S_3+S_4-6S_5)/15$. We retain the notation and definitions of these radial moments S_1–S_5 for the various intermediate and final states,

$$S=4\pi\sum_n\frac{\langle f|r|np\,{}^2P_j\rangle\langle np\,{}^2P_j|r|g\rangle}{\omega_{n,j}-\omega}, \tag{10}$$

as originally used by Lambropoulos and Teague [17]. $|f\rangle$ is one of the three outgoing channels $\varepsilon s\,{}^2S_{1/2}$, $\varepsilon d\,{}^2D_{3/2}$, or $\varepsilon d\,{}^2D_{5/2}$, and $j=1/2$ or 3/2 is the electronic angular momentum of the intermediate state. The initial, intermediate, and final states for the two-photon transitions corresponding to these five moments are given in Table I.

In order to define the total photoionization cross sections for the three channels, we integrate the angular distribution of Eq. (8) over all angles to yield

$$\sigma=\int\frac{d\sigma}{d\Omega}d\Omega$$

$$=\frac{m\alpha^2\omega^2|\vec{k}|}{\hbar}\Bigg\{\frac{1}{9}\left[\bar{S}_s^2+\frac{8}{25}\left(\frac{5S_3+S_4}{6}\right)^2+\frac{12}{25}S_5^2\right]$$

$$+\frac{1}{9}\left[\bar{S}_s^2-\frac{4}{25}\left(\frac{5S_3+S_4}{6}\right)^2-\frac{6}{25}S_5^2\right](\epsilon_1\epsilon_3^*-\epsilon_1^*\epsilon_3)^2\Bigg\}. \tag{11}$$

It has long been recognized that the cross section for two-photon ionization for the cases of linear and circular polarization differ [17]. Equation (11) is an extension of that result to the more general case of arbitrary polarization. For linear polarization the second term in Eq. (11) vanishes. The two-photon cross sections for photoionization into the $\varepsilon s\,{}^2S_{1/2}$, $\varepsilon d\,{}^2D_{3/2}$, and $\varepsilon d\,{}^2D_{5/2}$ channels, σ_s, $\sigma_{3/2}$, and $\sigma_{5/2}$, respectively, and the total cross section for the D wave, $\sigma_d=\sigma_{3/2}+\sigma_{5/2}$, by linearly polarized light in terms of the radial transition moments can be identified from Eq. (11) as

$$\sigma_s=\frac{m\alpha^2\omega^2|\vec{k}|}{\hbar}\frac{1}{9}\left(\frac{S_1+2S_2}{3}\right)^2,$$

$$\sigma_{3/2}=\frac{m\alpha^2\omega^2|\vec{k}|}{\hbar}\frac{8}{225}\left(\frac{5S_3+S_4}{6}\right)^2, \tag{12}$$

$$\sigma_{5/2}=\frac{m\alpha^2\omega^2|\vec{k}|}{\hbar}\frac{12}{225}S_5^2,$$

$$\sigma_d=\frac{m\alpha^2\omega^2|\vec{k}|}{\hbar}\frac{4}{45}\left(\bar{S}_d^2+\frac{3}{2}S_{\Delta d}^2\right).$$

In the absence of spin-orbit coupling in the intermediate or continuum states, $S_1=S_2$ and $S_3=S_4=S_5$. The latter relation yields $\sigma_{5/2}=1.5\sigma_{3/2}$, as can also be shown using state degeneracy arguments. For circular polarization, with $\pm i\epsilon_1=\epsilon_3=1/\sqrt{2}$, the polarization factor in Eq. (11) [i.e., $(\epsilon_1\epsilon_3^*-\epsilon_1^*\epsilon_3)^2$] becomes -1, and the excitation of the S wave vanishes, while the excitation rate of the D wave increases by a factor of 1.5 over that for linear polarization. For any other polarization state, the effective cross section for the partial waves lies between these two extremes.

Examples of three-dimensional photoelectron angular distributions for two-photon ionization, resulting from three different polarization states of the optical field, are shown in Fig. 2. These distributions correspond to (a) linearly polarized light, (b) right-elliptically-polarized light, and (c) circularly polarized light. In each case, the laser beam is propagating in a direction nearly normal to (into) the plane of the page (the $+\hat{y}$ direction). The distribution for linearly polarized light is symmetric about an axis parallel to the laser polarization (the $\hat{z}$ axis in Fig. 2), while that for circularly polarized light is symmetric about the axis defined by the laser propagation direction (the $\hat{y}$ axis). The symmetry of the angular distribution for elliptical polarization is reduced, but

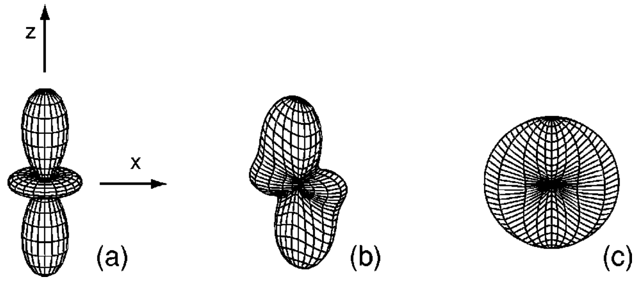

FIG. 2. Examples of calculated photoelectron angular distributions for (a) linearly polarized light, (b) right-elliptically-polarized light, and (c) circularly polarized light. These distributions represent the probability density for detecting a photoelectron as a function of angle. The direction of laser beam propagation is nearly into the plane of the page.

inversion symmetry about the origin is still evident. The asymmetry of this distribution reverses as the handedness of the elliptical polarization is reversed. The distributions for linear polarization and circular polarization are in complete agreement with those derived in Ref. [17].

In order to illustrate the advantage of using elliptically polarized light in multiphoton ionization measurements, specifically, its ability to constitute a complete photoionization measurement, it is instructive to reduce the very general expressions for $d\sigma/d\Omega$ given in Eqs. (8) and (9), valid for all angles Θ and Φ, to those for the restricted space of $\Phi=0$ or π, i.e., in the x-z plane, and with the limited polarization state defined earlier, $\epsilon_1=i\epsilon_1''$ and $\epsilon_3=\epsilon_3'$, where ϵ_1'' and ϵ_3' are real. (We remove our previous restriction that ϵ_1'' and ϵ_3' are positive, allowing the sign of $\epsilon_1''\epsilon_3'$ to indicate the sense of rotation of the field vector.) The angular distribution in this plane then takes the form

$$\begin{aligned}\frac{d\sigma}{d\Omega}=\frac{m\alpha^2\omega^2|\vec{k}|}{4\pi\hbar}\Bigg\{\Bigg|&\frac{1}{3}\left(e^{i\xi_s}S_s^- - e^{i\xi_d}S_d^-(3\cos^2\Theta-1)\right)\epsilon_3'^2\\&-2ie^{i\xi_d}S_d^-\sin\Theta\cos\Theta\,\epsilon_1''\epsilon_3'\\&-\frac{1}{3}\left(e^{i\xi_s}S_s^- + e^{i\xi_d}S_d^-(3\cos^2\Theta-2)\right)\epsilon_1''^2\Bigg|^2\\&+|-\sin\Theta\cos\Theta(\epsilon_3'^2+\epsilon_1''^2)\\&+i(2\cos^2\Theta-1)\epsilon_1''\epsilon_3'|^2S_{\Delta d}^2\Bigg\}.\end{aligned}\tag{13}$$

Evaluating this in a harmonic series yields

$$\frac{d\sigma}{d\Omega}=\frac{m\alpha^2\omega^2|\vec{k}|}{4\pi\hbar}a_0(1+a_2\cos 2\Theta+a_4\cos 4\Theta+b_2\sin 2\Theta),\tag{14}$$

where

$$\begin{aligned}a_0=&\frac{1}{9}\left(S_s^{-2}-S_s^-S_d^-\cos(\xi_s-\xi_d)+\frac{1}{4}S_d^{-2}\right)(\epsilon_3'^2-\epsilon_1''^2)^2\\&+\frac{1}{8}(S_d^{-2}+S_{\Delta d}^2)(\epsilon_3'^4+6\epsilon_1''^2\epsilon_3'^2+\epsilon_1''^4),\end{aligned}$$

$$a_2=\frac{1}{3a_0}[S_d^{-2}/2-S_s^-S_d^-\cos(\xi_s-\xi_d)](\epsilon_3'^4-\epsilon_1''^4),$$

$$a_4=\frac{1}{8a_0}(S_d^{-2}-S_{\Delta d}^2)(\epsilon_3'^2-\epsilon_1''^2)^2,$$

$$b_2=-\frac{2}{3a_0}S_s^-S_d^-\sin(\xi_s-\xi_d)\epsilon_3'\epsilon_1''(\epsilon_3'^2-\epsilon_1''^2).\tag{15}$$

The coefficient a_0 affects the overall amplitude of the photoelectron flux, but does not influence the shape of the angular distribution, which is described completely by the three coefficients a_2, a_4, and b_2. These last three coefficients are uniquely defined in terms of the ratios of reduced transition moments S_s^-/S_d^- and $S_{\Delta d}/S_d^-$, and the phase difference $\xi_s-\xi_d$, or equivalently σ_s/σ_d, $\sigma_{5/2}/\sigma_{3/2}$, and $\xi_s-\xi_d$. In the case of linear vertical polarization, corresponding to $\epsilon_3'=1$ and $\epsilon_1''=0$, the coefficient b_2 vanishes. This distribution is symmetric about the $\hat{z}$ axis, and a measurement of this distribution alone is sufficient for determining only two of the three atomic parameters. Furthermore, since this distribution depends only on $\cos(\xi_s-\xi_d)$ and not on the phase difference itself, an additional ambiguity results. Use of elliptical polarization (ϵ_3' and ϵ_1'' unequal, and each nonzero), however, yields an asymmetric angular distribution whose only symmetry is upon inversion about the origin. This yields one more fitting term (b_2) in the experimental determination, allowing for the simultaneous determination of all three of the atomic parameters. Since the asymmetry of this distribution reverses depending on the sign of $\sin(\xi_s-\xi_d)$, the determination of the phase difference (modulus π) is unambiguous as well. Additionally, if the sign of the product of two-photon moments $S_s^-S_d^-$ were known, then the determinations of the phase difference would be modulus 2π. A change of sign of this product, however, is equivalent to a π phase shift in $\xi_s-\xi_d$, so that in the absence of any knowledge of the relative signs of the moments we can determine $\xi_s-\xi_d$ only to within modulus π. Finally, it can be shown that the specialized angular distribution given by Eqs. (14) and (15), as well as the general form given by Eqs. (8) and (9), depend on $(S_{\Delta d}/S_d^-)^2$, but not $S_{\Delta d}/S_d^-$. For this reason, the sign of $S_{\Delta d}/S_d^-$ is undetermined in our measurements. We did not recognize this important aspect of these measurements when we prepared of our earlier report [15].

In the experiments we describe in this paper, we collect photoelectrons ejected in all directions, not limited to the x-z plane. These 4π solid angle distributions are, of course, also sensitive to the ellipticity of the laser polarization, and our measurements exploit this to make our complete determinations.

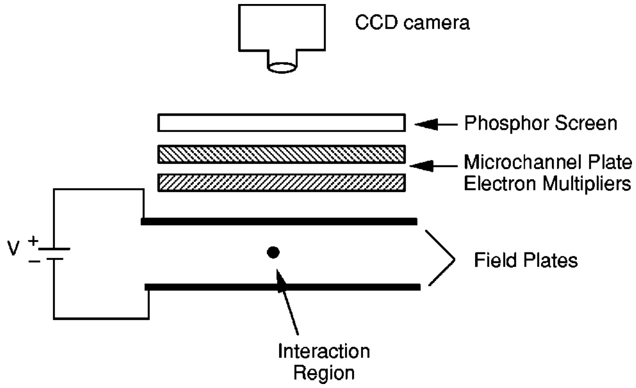

FIG. 3. Schematic diagram of the photoelectron imaging system.

III. PHOTOELECTRON COLLECTOR

In order to carry out these measurements, we required a photoelectron detector that would allow us to measure asymmetric angular distributions similar to that shown in Fig. 2(b). For this purpose we have adapted a technique introduced by Helm *et al.* [22] for measuring complete angular distributions of photoelectrons. The traditional technique (see Ref. [21], for example) for measuring photoelectron angular distributions is to photoionize the atoms in a field-free region, and to count the photoelectrons ejected toward a single-channel electron detector while rotating the laser polarization. One must ensure that, as the polarization is rotated, the laser beam does not move, the intensity does not vary, and the polarization does not change other than by a simple rotation. This traditional technique is characterized by a low collection efficiency, as only the photoelectrons ejected toward the single-channel detector are collected. With the Helm *et al.* apparatus, there is no need to rotate the polarization of the laser field, as the electrons ejected into the entire 4π steradian solid angle are collected with equal efficiency for each laser pulse. The detector, as shown schematically in Fig. 3, consists of a pair of parallel meshes (field plates) used to create a uniform electric field in the region surrounding the interaction region, two microchannel plate (MCP) electron multipliers, a phosphor screen, and a charge-coupled device (CCD) camera interfaced to a PC. The parallel meshes are very fine stainless steel screens (1 mil wires spaced by 10 mils) stretched tightly across 10 cm diameter frames. The separation between the meshes is $D=1.35$ cm. We obtained the MCP/phosphor screen assembly commercially. Electrons that escape from the atoms through photoionization by the laser field follow a parabolic trajectory due to their uniform acceleration in the static electric field toward the upper plate. Electrons transmitted through the upper mesh accelerate toward the microchannel plate electron multipliers, which provide a gain of $\sim 10^6$, and subsequently produce bright spots on the phosphor screen. The image is recorded by the camera and stored by the PC.

Several examples of photoelectron images are shown in Fig. 4. In each image, the laser beam propagates in the $+\hat{y}$ direction. [See the coordinate frame in Fig. 4(c)]. Each of these images can be understood by referring to the three-dimensional angular distributions shown in Fig. 2. For each of the three images corresponding to linear polarization in Figs. 4(a)–4(c), for example, the two maxima in the angular distribution along the direction of polarization and the ring in the direction perpendicular to the axis are clearly seen. With the linear polarization vertical [Fig. 4(a)], one maximum of the angular distribution is projected upward, the other downward. These two maxima overlap on the image screen directly above the interaction region, labeled M_u and M_l on the figure. The electrons comprising the ring around the waist initially travel radially outward in a horizontal plane. Due to the uniform field, they project onto the image plane to form a perfectly circular ring. With the laser polarization still linear, but rotated 45°, the two maxima separate, as seen in Fig. 4(b). The upper maximum (M_u) is shifted slightly to the left, but still forms a well-defined image. The electrons in the lower maximum (M_l) initially propagate down and to the right in the uniform field region, but have more time to spread out before reaching the image plane, as their vertical velocity must reverse direction. The ring, while not perfectly circular in the image plane, is clearly visible in the diagram as well. The final sample image for linear polarization is shown in Fig. 4(c), corresponding to horizontal polarization. In this case the two maxima (*M*) form symmetrically placed spots on the left and right edges, while the ring forms a single band in the center. The images for elliptical polariza-

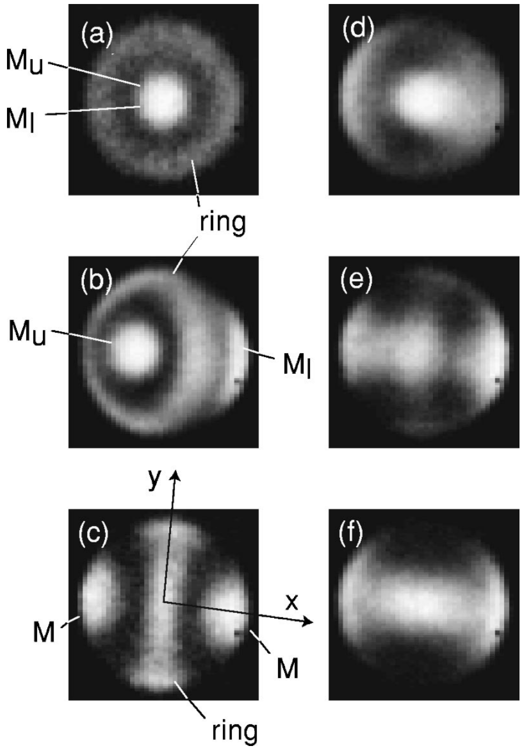

FIG. 4. Several examples of images created by the photoelectrons on the phosphor screen for different polarizations of light. The polarizations are (a) linear, vertical, (b) linear, 45° from vertical, (c) linear, horizontal, (d) left-elliptical, major axis vertical, (e) left-elliptical, major axis horizontal, and (f) circular. (The dark mark in the lower right quadrant of these images is a damaged spot on the phosphor screen.)

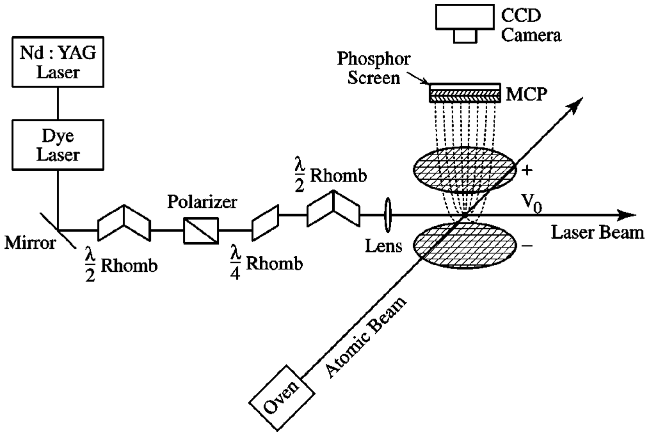

FIG. 5. Schematic diagram of the optical system and detection apparatus.

tion are slightly more complex, but clearly display the asymmetry that might be expected of the angular distributions shown in Fig. 2(b). The major axis of the ellipse is vertical for Fig. 4(d) and horizontal for Fig. 4(e). In each case, the dark band of the image results from the local minimum in the upper side of the distribution. For the image generated by circularly polarized light, the doughnut-shaped angular distribution projects onto the phosphor screen to create a single band, as seen in Fig. 4(f).

For quantitative analysis of the image displayed on the phosphor screen we must map the parabolic trajectory of the photoelectrons from the interaction region to the phosphor screen. The primary result of this analysis, details of which we present in the Appendix, allows us to accurately determine the image formed on the phosphor screen for any given angular distribution of the photoelectrons. The inverse of this operation, i.e., determining the photoelectron angular distribution from the image, can also be carried out, if the angular distribution is symmetric upon inversion about the origin, as is the case for the present measurements. Coupled with the theory for the photoelectron distributions, we are thus able to use the photoelectron images produced by this detector to accurately determine the three atomic parameters we seek.

IV. EXPERIMENT

A schematic of the experimental setup is shown in Fig. 5. The atomic beam geometry is necessary to limit the volume of the interaction region, defined by the intersection of the laser beam and the atomic beam. The vacuum system consists of two separately pumped chambers, one housing an effusive oven that generates the atomic beam, and the other containing the interaction region. The two chambers are separated by a stainless steel plate with a 4 mm diameter hole at the center. The small hole allows only a fraction of the rubidium atoms to pass into the interaction chamber, reducing the background noise at the detector. The oven is maintained at a body temperature of 145 °C. The nozzle, with an aperture diameter of 0.9 mm, is held at a slightly elevated temperature to discourage rubidium condensation and dimer formation. The oven produces an atomic beam density of 3×10^{7} cm^{-3} at the interaction region, a distance of $\sim$37 cm from the oven aperture. A second aperture just before the interaction region limits the beam diameter to 0.66 mm. The vacuum chamber housing the interaction region is pumped to a level of 2×10^{-8} torr using a cryogenic pump. We cancel the earth's magnetic field to less than 10 mG in the interaction region using three orthogonal pairs of coils.

The laser sources for this work include a *Q*-switched, frequency-doubled Nd:YAG (yttrium aluminum garnet) laser and a pulsed dye laser system. The dye laser consists of an oscillator and a three-stage amplifier, each pumped by the 532 nm second-harmonic output of the YAG system. The laser oscillator is a short-cavity, longitudinally pumped Littman configuration [23], with the output limited to 1–3 longitudinal modes in a nearly-lowest-order Gaussian transverse mode. We use the dye laser system to generate light at eight different wavelengths between 540 nm and 590 nm, employing three different laser dyes (Fluorescein 548, Rhodamine 590, and Rhodamine 610) to cover this wavelength range. We determine the wavelength of the light using a quarter-meter monochromator, calibrated with a He-Ne laser at 632.8 nm and the 532 nm harmonic output of the Nd:YAG laser. We also carry out our photoionization measurements with the $\lambda=532$ nm harmonic light directly.

The polarization of the optical field is critical for these measurements. We control the polarization using the optical components shown in Fig. 5. Most of our measurements are carried out using left-elliptically-polarized light, which we generate by rotating the first $\lambda/2$ Fresnel rhomb in the figure by 11.25° and the polarizer by 22.5°, each in the clockwise direction. (We describe all rotations as viewed by an observer looking into the laser source.) The $\lambda/4$ rhomb, oriented vertically as shown in the figure, changes the polarization of the exiting light to right elliptical. The handedness of the ellipticity can be determined only by considering the difference in the phase shifts of the *S*- and *P*-polarized components resulting from the two total internal reflections in the $\lambda/4$ Fresnel rhomb. Born and Wolf [18] show that the *P*-polarized (vertical) component is advanced relative to the *S*-polarized (horizontal) component, so that light entering the rhomb with polarization $\hat{\epsilon}=\sin 22.5°\hat{x}-\cos 22.5°\hat{z}$ exits the rhomb as right-elliptically-polarized light, $\hat{\epsilon}=-i\sin 22.5°\hat{x}+\cos 22.5°\hat{z}$, with the major axis vertical. The final $\lambda/2$ Fresnel rhomb, when oriented at 45° from the vertical, rotates the ellipse by 90° and reverses the rotation sense. The major axis of the elliptical polarization is thus horizontal, and the sense of the rotation is left handed, $\hat{\epsilon}=i\cos 22.5°\hat{x}+\sin 22.5°\hat{z}=i|\epsilon_1|\hat{x}+|\epsilon_3|\hat{z}$. The two measurements taken with right-elliptically-polarized light were obtained by rotating the first $\lambda/2$ rhomb and polarizer in the counterclockwise direction. We also carried out measurements at each wavelength using linear polarization, oriented either at 45° from the vertical or horizontally. To obtain linear polarization at 45° from the vertical, we keep the first $\lambda/2$ rhomb and polarizer oriented vertically, as shown in the figure, and rotate the final $\lambda/2$ rhomb 22.5° from vertical in the counterclockwise direction. Similarly, for linear horizontal polarization, we rotate the final $\lambda/2$ rhomb to an angle of 45° from verti-

TABLE II. Experimental parameters for each wavelength.

λ (nm)	ε (meV)	V (V)	Number of shots	ϵ_3/ϵ_1	Pulse energy (mJ)	Image radius (cm)
590.0	26	0.05	8000	$+0.438i$	1.3	0.55
583.3	74	0.40	8000	$+0.437i$	1.3	0.65
583.3	74	0.40	8000	$-0.437i$	1.3	0.65
575.0	135	0.65	8000	$-0.435i$	1.3	0.82
568.2	187	1.0	25000	$-0.433i$	2.5	0.80
560.0	251	1.4	10000	$-0.431i$	2.5	0.79
553.0	307	1.8	10000	$-0.429i$	2.5	0.77
547.0	356	2.2	25000	$-0.427i$	2.5	0.81
540.0	415	2.2	10000	$-0.426i$	2.5	0.86
532.0	484	2.6	10000	$-0.424i$	2.5	0.88

cal. We insert an additional linear polarizer after the final rhomb to improve the polarization purity. For each polarization state we confirm the polarization of the field by measuring the transmission of the beam through a Glan-laser polarizer and recording the transmission as a function of the polarizer orientation θ'. For elliptical polarization, we fit the result to the function

$$P_t = P_0(|\epsilon_1|^2 \sin^2\theta' + |\epsilon_3|^2 \cos^2\theta'). \tag{16}$$

We find that the typical rms deviation between the measured transmitted power and the best fit function of the form of Eq. (16) is ~1% of the maximum transmitted power. While this measurement is insensitive to the handedness of the polarization, it does allow us to determine very precisely the magnitude of the ellipticity. We measured ϵ_3/ϵ_1 at five different wavelengths between 532 nm and 591 nm, and fitted a linear function to these measurements. We observe a slight variation of ϵ_3/ϵ_1 with wavelength, which is reasonable in that the phase shift induced upon total internal reflection within the Fresnel rhombs is somewhat wavelength dependent.

The dye laser beam is weakly focused to an e^{-2} radius of approximately 0.30 mm in the interaction region, as determined by measuring the transmission through a 0.254 mm diameter pinhole. We estimate the peak laser intensity to be on the order of 0.2 $\mathrm{GW\,cm^{-2}}$ when the laser pulse energy is 2.5 mJ. At each wavelength, we accumulate an image over 8000–25 000 laser pulses, with each image consisting of approximately 10^5 electrons. The photoelectron kinetic energy ε, the voltage applied between the meshes V, the total number of laser pulses, the polarization ellipticity, the laser pulse energy, and the image radius $r'_{\max}$ are given for each wavelength in Table II. With an interaction volume of $\sim 10^{-4}$ cm^3, there are about 3×10^3 atoms in the interaction region. We detect approximately 10–20 electrons for every laser pulse. An example of the raw image of the phosphor screen corresponding to a single laser pulse is shown in Fig. 6. The horizontal axes indicate the pixel indices of the 64×128 image. The vertical axis is the recorded signal strength of each pixel in the array. Each peak in the image contains about 6–12 bright pixels and corresponds to a single electron. We purposely maintain this electron count at a low level so as to minimize the possibility of overlapping electrons on the phosphor screen, space charge effects, which could perturb the parabolic trajectory of the photoelectrons as they travel toward the upper mesh plate, and high-field effects, which would change the atom-field interaction.

In order to decrease the influence of any gain nonuniformities of the microchannel plate detector, the phosphor screen, or the CCD array in the camera, we employ a threshhold detection scheme. In this scheme, each bright cluster in the raw image is regarded as one count, regardless of the height or area of the peak. A computer algorithm locates the center of mass of each bright spot in the image, and records one electron at the pixel closest to the center of the cluster. The PC is able to analyze the image for each laser pulse in this way, and add the result to the accumulated image in less than 0.1 s, the time between successive laser pulses. This detection scheme proves to be essential in our measurements, as the image distortions introduced by the irregularities of the detector mentioned above are prohibitive. For example, the images shown in Fig. 4 were collected in a linear accu-

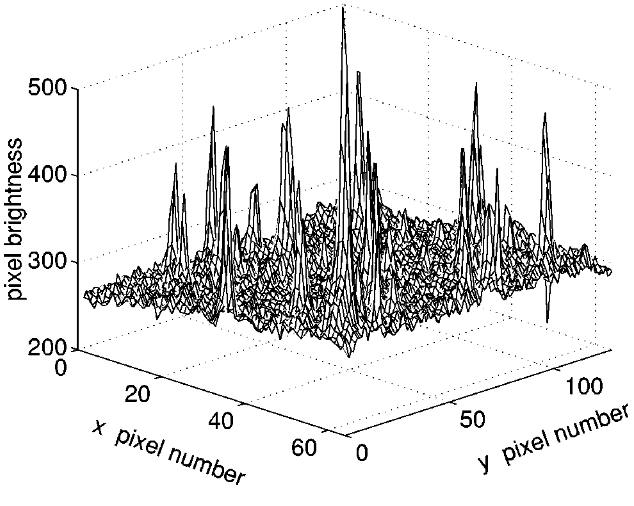

FIG. 6. A sample image of the phosphor screen resulting from a single shot of the laser. The horizontal axes indicate the pixel indices of the 64×128 image. The vertical axis is the recorded signal strength of each pixel in the array. Each peak in the image corresponds to a single electron.

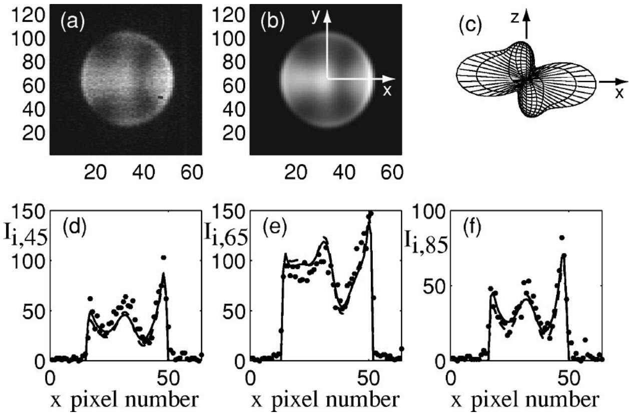

FIG. 7. Typical photoelectron distribution for left-elliptically-polarized light. These data represent the accumulated image after 10 000 laser pulses at a wavelength of $\lambda = 540$ nm. The measured two-dimensional image is shown in (a), while in (b) we show the calculated image based on the best fit atomic parameters. The angular distribution that produces this image is shown in (c). Three cross-sectional slices are shown in the remaining sections, corresponding to rows 45, 65, and 85 of the images shown in (a) and (b). In each cross section, the data points are shown as dots, while the results of a least-squares fitting procedure are shown as the solid line. The dashed line shows the best fit curve if we restrict $S_{\Delta d}$ to a value of 0.

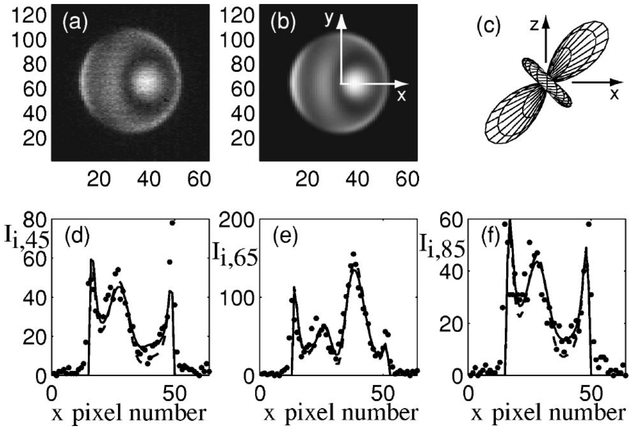

FIG. 8. Typical photoelectron distribution for linearly polarized light at 45° from vertical. These data represent the accumulated image after 10 000 laser pulses at a wavelength of $\lambda = 540$ nm. The measured two-dimensional image is shown in (a), while in (b) we show the theoretical image using cross sections and phases determined using elliptically polarized light. Three cross-sectional slices of the images shown in (a) and (b) are shown in the remaining subplots, rows (d) 45, (e) 65, and (f) 85. In the cross sections, the data points are shown as dots, while the calculated signal strengths are shown as solid lines. The dashed line shows the curve for $S_{\Delta d} = 0$.

mulation scheme, in which we simply sum the images pixel by pixel over a large number of laser pulses. While the images in this figure appear to be reasonable qualitatively, they could not be fitted well by any of our theoretical images. The threshold detection scheme is critical for quantitative comparisons.

We show examples of photoelectron images collected with the threshhold detection scheme in Figs. 7(a) and 8(a). Figure 7(a) corresponds to a left-elliptically-polarized laser beam at $\lambda = 540.0$ nm with the ellipticity (ϵ_3/ϵ_1) of the laser polarization equal to $-0.426i$, while for Fig. 8(a) the polarization is linear at 45° from vertical, $\epsilon_3/\epsilon_1 = +1$. The axes are labeled with the pixel indices 1–128 in the $\hat{y}$ direction and 1–64 in the $\hat{x}$ direction. (The pixels of the CCD camera sensor array are approximately square, but the camera transfers only alternate columns of data. Therefore there are only half as many columns of data as rows.) The direction of propagation of the laser beam $(+\hat{y})$ is from the bottom to the top of this figure, and the image is nearly symmetric with respect to the horizontal axis through the image's center. Since photoelectron angular distributions are symmetric upon inversion about the center (except in special cases involving interferences, as described in Ref. [24], for example), we expect the integrated photoelectron signal of the left and right half planes of the image to be equal, even though the images themselves are asymmetric. We find that the integrated signal of these half planes, found by summing the pixel values in each half plane, match one another to within 2% in all cases. Finally, the radius of the image on the phosphor screen is a good indicator of the experiment. We typically used an image radius of ~ 1 cm, chosen to be much greater than the size of the interaction region, but smaller than the size of the plane meshes that produce the uniform collecting field. We observed some evidence of an additional charge buildup or a bias on one of the field plates, producing an apparent offset of about 0.2 V to the voltage we applied. When we adjust the applied voltage by this offset, the measured radius of the image matches to within 5% the radius computed on the basis of the photoelectron kinetic energy, the strength of the dc collecting electric field, and the position of the interaction region, as expressed in Eq. (A7). This offset has a substantial effect only on the low-kinetic-energy electrons, and we observed no evidence of distortions of the images for any of the data sets.

V. DISCUSSION

For each image collected using elliptically polarized light, we select a trial set of photoionization two-photon moments and phases and compute the corresponding theoretical image. We adjust several underdetermined experimental parameters (the location of the center of the image, the distance d between the top mesh and the interaction region, the voltage V applied between the meshes, a parameter that represents the size of the interaction region, and a scaling factor) within a reasonable range to obtain the smallest root-mean-square deviation between the theoretical image and the measured image, as computed over all pixels in the image. All pixels are weighted equally in determining the rms deviation. We iterate repeatedly with new choices of S_s^-/S_d^-, $S_{\Delta d}/S_d^-$, $\xi_s - \xi_d$, and the experimental parameters listed above in order to find the set that produces the image in best agreement with the measured image. We choose step sizes of 0.02 between

TABLE III. Relative two-photon moments, cross sections for two-photon absorption, and continuum wave function phase differences as determined from the photoelectron images.

λ (nm)	S_s^-/S_d^-	$\lvert S_{\Delta d}/S_d^-\rvert$	σ_s/σ_d	$\sigma_{5/2}/\sigma_{3/2}$		$\xi_s-\xi_d$ (rad)
				$S_{\Delta d}/S_d^- > 0$	$S_{\Delta d}/S_d^- < 0$	
590.0	−0.55(2)	0.35(2)	0.32(3)	0.27(3)	12(3)	2.36(7)
583.3	−0.47(2)	0.33(2)	0.25(3)	0.30(3)	11(3)	2.34(6)
575.0	−0.45(2)	0.32(2)	0.22(3)	0.32(3)	10(3)	2.25(6)
568.2	−0.40(2)	0.32(2)	0.18(2)	0.32(3)	9(2)	2.15(4)
560.0	−0.42(2)	0.36(2)	0.19(2)	0.26(3)	14(2)	2.08(4)
553.0	−0.43(2)	0.34(2)	0.20(2)	0.29(3)	11(2)	1.98(4)
547.0	−0.38(2)	0.36(2)	0.15(2)	0.26(3)	13(2)	2.02(4)
540.0	−0.39(2)	0.35(2)	0.16(2)	0.27(3)	12(2)	1.96(4)
532.0	−0.38(2)	0.34(2)	0.15(2)	0.29(3)	11(2)	1.85(4)

trial values for S_s^-/S_d^-, $S_{\Delta d}/S_d^-$, and $\xi_s-\xi_d$. The results of this iterative procedure are listed in Table III. The fitting procedure accommodates the lateral dimensions of the interaction region, but not the vertical.

Using the best fit values of S_s^-/S_d^- and $S_{\Delta d}/S_d^-$, we also determine the cross-section ratios σ_s/σ_d and $\sigma_{5/2}/\sigma_{3/2}$, using

$$\sigma_s/\sigma_d=\frac{5}{4}\left(\frac{(S_s^-/S_d^-)^2}{1+\frac{3}{2}(S_{\Delta d}/S_d^-)^2}\right) \tag{17}$$

and

$$\sigma_{5/2}/\sigma_{3/2}=\frac{3}{2}\left(\frac{1-S_{\Delta d}/S_d^-}{1+\frac{3}{2}S_{\Delta d}/S_d^-}\right)^2, \tag{18}$$

as determined from Eqs. (12). These relative cross sections are also presented in Table III. Since the sign of $S_{\Delta d}/S_d^-$ cannot be ascertained from our measurements, we report two possible values of $\sigma_{5/2}/\sigma_{3/2}$. Positive $S_{\Delta d}/S_d^-$ yields a ratio $\sigma_{5/2}/\sigma_{3/2}$ which is less than 1.5, while $\sigma_{5/2}/\sigma_{3/2}>1.5$ is the result if $S_{\Delta d}/S_d^-$ is negative. Some of the present results differ slightly from the results we reported in Ref. [15]. The present results are more accurate, due to improved fits between the calculated and measured images.

The best fit image to the data of Fig. 7(a) is shown in Fig. 7(b). The calculated angular distribution that produces this image is shown in Fig. 7(c). Cross-sectional slices for single rows [row 45 in (d), 65 in (e), and 85 in (f)] of the image, showing the best fit results (solid lines) and measurements (data points), are also shown in Fig. 7. The root-mean-square deviations of these data are somewhat larger than those expected for a Poisson process, as we determine by computing χ^2 for the fits. In computing χ^2, we use $\sqrt{I_{i,j}}$ as the standard deviation of each pixel value of the image, where $I_{i,j}$ is the image value of pixel (i,j). This is justified in the threshold detection scheme we described earlier, in that $I_{i,j}$ is the number of photoelectrons at that point in the image. We find χ^2 ranges from 1.5 to 2.3 for each image, where $\chi^2=1$ would indicate purely statistical counting errors. One contribution leading to χ^2 values greater than unity is a slight variation in the signal strength of individual rows of data, possibly caused by a nonuniformity of the geometric areas in different rows of the CCD array of the camera.

We show two-dimensional (*x*-*z* plane) angular distributions calculated using the atomic parameters in Table III and the ellipticities from Table II for three wavelengths (590 nm, 560 nm, and 532 nm) in Fig. 9(a). As the optical wavelength decreases, the relative photoelectron flux along the *x* axis increases, and the distribution becomes more elongated.

In order to estimate the uncertainty in the results shown in Table III we collected two of the data sets (at λ = 568.2 nm and λ = 547.0 nm) as five separate, consecutive runs of 5000 laser shots each. We then fitted each image individually in order to determine the distribution of the fitted results. The reproducibility of the fits to the images was in fact very good, yielding uncertainties that were comparable to or smaller than the step sizes of the various parameters.

The sense of rotation of the elliptically polarized light was left in all cases except two. For λ = 590.0 nm we recorded the photoelectron image corresponding to right-elliptical polarization only, while for λ = 583.3 nm we recorded the photoelectron image corresponding to left- and right-elliptical polarization. (See Table II.) As predicted by theory, the asymmetry of the image reversed. For λ = 583.3 nm the best fit values of σ_s/σ_d, $\sigma_{5/2}/\sigma_{3/2}$, and $\xi_s-\xi_d$ resulting from the two data sets are in agreement within estimated uncertainties.

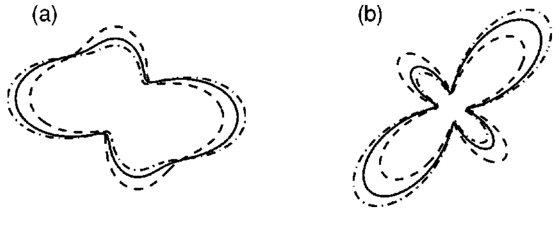

FIG. 9. Two-dimensional photoelectron angular distributions for (a) elliptically polarized light and (b) linearly polarized light (oriented along the long axis at 45°) calculated using the cross-section ratios and phase differences given in Table III. The three lines correspond to λ = 590.0 nm (dashed), λ = 560.0 nm (solid), and λ = 532.0 nm (dot-dashed).

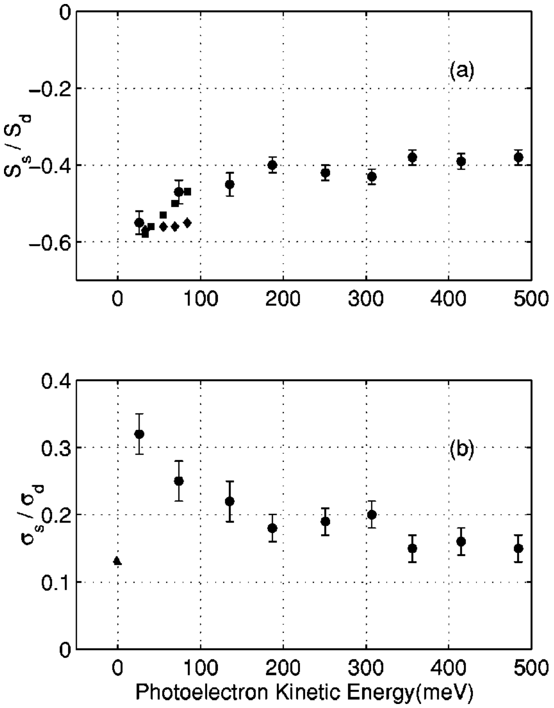

FIG. 10. The ratio of (a) two-photon moments S_s^-/S_d^- and (b) cross sections σ_s/σ_d versus photoelectron kinetic energy. The square data points and the diamond-shaped data points in (a) are the results of calculations of cross sections based on a Sturmian basis set [25] and Hartree-Fock basis set [26], respectively. The circular data points are the results of the present work. The triangular data point in (b) is obtained from a spectrum shown in Ref. [12].

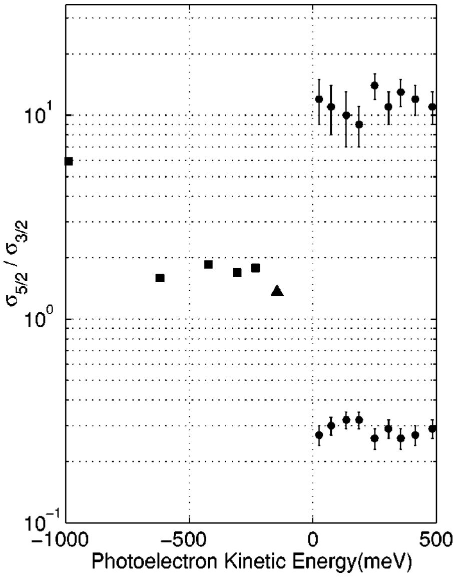

FIG. 11. The ratio of cross sections $\sigma_{5/2}/\sigma_{3/2}$ versus photoelectron kinetic energy. The circular data points are the results of the present work. The triangular data point is obtained from a bound state spectrum shown in Ref. [12]. The square data points are as reported in Ref. [11].

As we discussed earlier, the linear-polarization data do not constitute a complete measurement, and therefore are not sufficient to allow us to determine the photoionization cross sections and continuum phase differences. We should expect, however, that the cross sections and phases that we determine using elliptically polarized light will enable us to predict the linear-polarization angular distributions. This expectation is fulfilled, as can be seen in Fig. 8. The measured data are shown in Fig. 8(a), the calculated image in Fig. 8(b), and the corresponding angular distribution in Fig. 8(c). We show the measured data points (circles) and the theoretical curves (solid line) for three rows [row 45 in (d), 65 in (e), and 85 in (f)] of the image. The only parameters that we adjusted in these calculated images are the amplitude of the signal and the size and position of the image. We determined all other parameters from the elliptically polarized data. This close agreement is characteristic of that observed for each data set using linear polarization, for which the rms deviation of the data and theory is in the 6–12 % range. χ^2 for these images ranges from 1.7 to 2.5. We show two-dimensional (x-z plane) angular distributions corresponding to linear polarization (with the laser polarization at 45° from vertical) for three wavelengths in Fig. 9(b). These plots are based upon the experimentally determined atomic parameters presented in Table III. At the longest wavelength, the ring around the waist is nearly as large as the maximum flux along the laser polarization. As the wavelength decreases, however, the side ring shrinks relative to the maximum. These plots are very consistent with those that we reported in Ref. [8].

We show plots of S_s^-/S_d^- vs ε and σ_s/σ_d vs ε in Fig. 10. The relative cross section of the s wave decreases with increasing photoelectron energy to an energy of about 200 meV, beyond which there is relatively little change. In addition to data from the present work (circular data points), we also show two sets of theoretical results in (a) and an additional experimental data point in (b). The theoretical data points were reported as asymmetry parameters for photoelectron angular distributions from atomic rubidium, which we converted to relative two-photon moments and continuum phase differences. The calculations of S_s^-/S_d^- were based on a Sturmian basis set (squares) [25] and a Hartree-Fock basis set (diamonds) [26], respectively. We see that the agreement of these theoretical results and our experimental points is very good. The energy dependence of the Sturmian basis points is also in good agreement over the limited range of those results. We were also able to extract an estimate of σ_s/σ_d from a bound state spectrum presented in Ref. [12]. This point comes from two-photon absorption at $\lambda = 593.83$ nm, showing peaks corresponding to excitation of the 100d and 102s states, and its uncertainty is perhaps as large as 25% owing to the small amplitude of the 102s peaks [27]. We used only the relative peak heights for this estimate, rather than the peak area. Any differences in these widths would alter this estimate. A discontinuity at $\varepsilon = 0$ in σ_s/σ_d, if it is real, should not be expected. The results of Ref. [8] (not shown in Fig. 10), in which we used photoelectron angular distributions for linearly polarized light supplemented by semiempirical phases to determine σ_s/σ_d, are roughly consistent with the present data.

In Fig. 11 we show a plot of $\sigma_{5/2}/\sigma_{3/2}$ vs ε. We show two data sets in this figure, corresponding to columns 5 and 6 in Table III, since our experimental results are not capable of determining the sign of $S_{\Delta d}/S_{\bar{d}}$. The uncertainty in the data points is comparable to their difference, so that no clear energy dependence is observed. Also shown in Fig. 11 are data points corresponding to bound state spectra from previous works [11,12]. These values of intensity ratios correspond to two-photon $5s\,^2S_{1/2}\rightarrow nd\,^2D_{3/2,5/2}$ transitions, for $n=5$ through 9 (squares) and $n=11$ (triangle). The data point at $\varepsilon=-990$ meV is elevated due to the near one-photon resonance of the laser with the $5s\rightarrow 5p$ transition. The discontinuity between the bound state ratios and the continuum state ratios is quite surprising, and will require further study to understand. The results of Ref. [8] for $\varepsilon>0$ also suggested that the ratio $\sigma_{5/2}/\sigma_{3/2}$ differed significantly from 1.5. While the present results confirm this qualitative conclusion, the present measurements yield ratios of $\sigma_{5/2}/\sigma_{3/2}$ that consistently deviate from 1.5 even more than those of Ref. [8]. In view of the dependence of the analysis of Ref. [8] on various assumptions, we regard the present results as the more reliable determination of this ratio in the continuum.

It is reasonable to ask to what extent the fit between the measured image and the calculated image is diminished if we restrict $S_{\Delta d}$ to a value of zero. An example of these fits is shown as the dashed lines in Figs. 7 and 8. The off-center curves [rows 45 (d) and 85 (f)] with $S_{\Delta d}=0$ show deeper minima than do the corresponding curves with $S_{\Delta d}$ at its best fit value. The effect is more evident for the linear polarization data than for elliptical polarization. While the difference between the curves can be subtle, the quality of the fit is clearly poorer for the $S_{\Delta d}=0$ curve, and the difference between these curves is statistically significant.

The effect of the spin-orbit interaction on the intensity ratios of the fine structure components of linear absorption lines [28] has been studied in great detail for rubidium [29–31]. For example, the ratio of oscillator strengths, $\rho=f_{3/2}/f_{1/2}$, for the principal series ($5s\,^2S_{1/2}\rightarrow np\,^2P_{1/2,3/2}$) in rubidium is known to increase rapidly with increasing n from $\rho\sim 2$ for $n=5$ to $\rho\sim 4$ or 5 for $10<n\leqslant 20$. Oscillator strengths for the fine structure components of the sharp ($5p\,^2P_{1/2,3/2}\rightarrow ns\,^2S_{1/2}$) and diffuse ($5p\,^2P_{1/2,3/2}\rightarrow nd\,^2D_{3/2,5/2}$) series have also been measured [30] and calculated [31]. One can estimate the ratio of two-photon absorption cross sections $\sigma_{5/2}/\sigma_{3/2}$ from the latter series, yielding a ratio of between 1.5 and 1.7 up to $n=10$. The shortcoming of this estimate, of course, is that it ignores all contributions of intermediate mp states for $m>5$. These additional contributions could significantly modify the relative two-photon cross sections, even if there are no anomalies in the $mp\rightarrow nd$ line strength intensity ratios, with their sign determining whether $\sigma_{5/2}/\sigma_{3/2}$ is greater than or less than 1.5. This spin-orbit effect should manifest itself in the doublet line strength ratios measured in the bound state spectra, as well as in the continuum measurements reported in this work, so it is not clear how this difference in $\sigma_{5/2}/\sigma_{3/2}$ between $\varepsilon<0$ and $\varepsilon>0$ can be explained.

In Fig. 12, we plot the results of our determination of the continuum phase difference as a function of the kinetic energy of the photoelectron, ε. For comparison, we also show the phase difference as given by the sum of Eqs. (5) and (6) (solid line), and as data points the phase differences that we extract from the theoretical results of Refs. [25] and [26]. We see from the figure that there is very good agreement between the experimental determinations and the theoretical values of the phase difference, providing direct experimental confirmation of this term over the entire range of photoelectron kinetic energies of our observations. The agreement of these results with the expected phase difference lends considerable confidence to our technique and to our unexpected values for $\sigma_{5/2}/\sigma_{3/2}$.

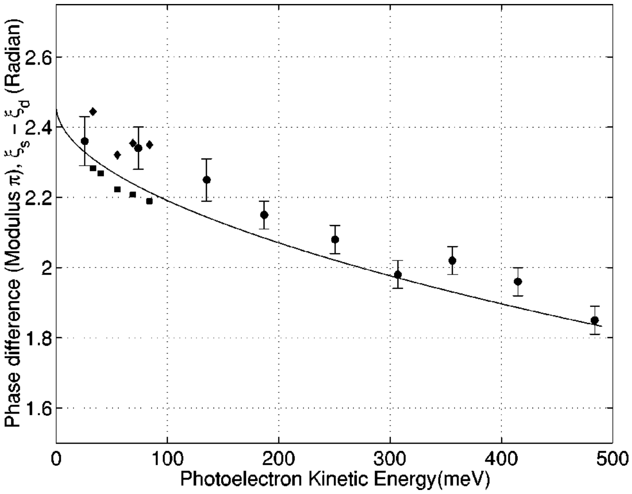

FIG. 12. The phase difference between continuum $\varepsilon\,^2S$ and $\varepsilon\,^2D$ wave functions, $\xi_s-\xi_d$, in atomic rubidium. The solid line represents the results of Eqs. (5) and (6). The square data points and the diamond-shaped data points are the results of calculations of phase differences based on a Sturmian basis set [25] and a Hartree-Fock basis set [26], respectively.

In this paper, we have demonstrated that, by using elliptically polarized light, measurements of two-photon photoelectron angular distributions of rubidium comprise a complete determination of the relative atomic cross sections and continuum function phase differences necessary to describe this interaction. This represents a clear advance over similar measurements based upon linearly polarized light, or based upon simultaneous measurements such as angular distributions and spin polarization of the photoelectron. We report continuum wave function phase differences that appear to be in excellent agreement with expected values, as well as relative cross sections to the S and D continua. The ratio of cross sections $\sigma_{5/2}/\sigma_{3/2}$, however, differs significantly from 1.5, a result we find surprising in light of bound state ratios reported previously [11,12]. Spin-orbit interactions may be responsible for this effect [28], but it is unexpected that such an effect would be dominant in one energy range but absent in an adjacent energy range. This inconsistency will require further study. We hope that these results will motivate calculations of two-photon cross sections in the discrete as well as in the continuum regions of the absorption spectrum for rubidium.

ACKNOWLEDGMENTS

This work was supported by the National Science Foundation. We gratefully acknowledge the contributions of T. Jackson and M. Crogan who wrote the computer programs necessary for the acquisition of these data, and helpful discussions with W. Hill and Jie Zhu concerning the construction and operation of the photoelectron detector, careful explanations of sign conventions of phases by F. Robicheaux, and helpful discussions with James Colgan concerning relative partial cross sections for photoionization of rubidium.

APPENDIX: MAPPING THE TRAJECTORY OF PHOTOELECTRONS

In this Appendix, we present our analysis of the trajectory of the photoelectrons as they travel from the interaction region, ejected at an initial angle (Θ,Φ), to the position at which they strike the phosphor screen. The photoelectrons start with an initial velocity $\sqrt{2\varepsilon/m}$, where ε and m are the initial kinetic energy and the mass of the photoelectron, respectively, and travel a transverse distance r' before encountering the upper mesh, where r' is determined by the conditions

$$d=\sqrt{\frac{2\varepsilon}{m}}\cos\Theta' t+\frac{eV}{2mD}t^2 \tag{A1}$$

and

$$r'=\sqrt{\frac{2\varepsilon}{m}}\sin\Theta' t. \tag{A2}$$

$D=1.35$ cm is the spacing between the mesh plates, V is the potential difference between the plates, $d\simeq 0.55$ cm is the distance between the upper mesh plate and the interaction region, e is the electronic charge, and t is the time required for the electrons to reach the upper mesh. In our experimental geometry, the angle between the initial momentum of the photoelectron and the applied collecting field, Θ', is the same as the polar angle of the momentum in the atomic frame, Θ, and we therefore drop the prime notation. Equations (A1) and (A2) can be combined to determine the transverse distance r' as a function of the experimental parameters and Θ,

$$r'=\frac{2\varepsilon D}{eV}\sin\Theta\left(\sqrt{\cos^2\Theta+\frac{eVd}{\varepsilon D}}-\cos\Theta\right). \tag{A3}$$

Upon inversion, this yields

$$\Theta=\frac{1}{2}\left[\arctan(r'/d)\pm\arccos\left(\frac{1-(eVd/2\varepsilon D)(r'/d)^2}{\sqrt{1+(r'/d)^2}}\right)\right], \tag{A4}$$

which shows that two values of Θ map into each r', as expected for parabolic trajectories. In our apparatus, $eVd/\varepsilon D$ typically has a value of approximately 2, so that electrons ejected at an angle Θ and those ejected at an angle $\pi-\Theta$ strike the phosphor screen at different locations r'. This is critical for the present measurements, as we must preserve the asymmetry of the photoelectron angular distribution created by the interaction of the atoms with the elliptically polarized light in the two-dimensional image generated on the phosphor screen. For comparison, the detector employed by Helm *et al.* [22] used a large accelerating voltage applied between the meshes, so that $eVd/\varepsilon D\gg 1$. Under these conditions, one observes nearly symmetric images, even for asymmetric angular distributions.

After passing through the mesh, the electrons are rapidly drawn to the microchannel plate multiplier by the 95 V potential difference between the bottom side of the MCP and the upper mesh, which are separated by only ~ 5 mm, allowing us to safely ignore any further transverse motion of the electrons. r' is therefore the distance we measure on the phosphor screen from the center of the image.

The magnitude of the average signal detected by each pixel of the CCD camera is given by

$$\begin{aligned} I_{i',j'}&=\int_V dV\int_t dt\,\frac{d\sigma}{d\Omega}\left|\frac{d\Omega}{dA'}\right|\Delta A' F^2(\vec{r},t)\rho_{at}\\ &\approx\frac{d\sigma}{d\Omega}\left|\frac{d\Omega}{dA'}\right|\Delta A'\int_V dV\int_t dt F^2(\vec{r},t)\rho_{at}, \end{aligned} \tag{A5}$$

where $d\sigma/d\Omega$ is the magnitude of the photoelectron angular distribution in the direction that maps into the pixel of the CCD camera of indices i',j', $|d\Omega/dA'|\Delta A'$ is the solid angle in the atomic frame that maps into the pixel area $\Delta A'$, $F(\vec{r},t)$ is the photon flux in the interaction region (in photons $\mathrm{cm}^{-2}\,\mathrm{s}^{-1}$), and ρ_{at} is the density of the atomic beam. The integrals are taken over the entire interaction volume and the pulse duration. The approximation in Eq. (A5) is valid when the interaction volume is small, allowing us to pull the $d\sigma/d\Omega$ and $|d\Omega/dA'|\Delta A'$ outside the integrals. $d\Omega/dA'$ is determined by differentiating Eq. (A3), yielding

$$\begin{aligned} \frac{d\Omega}{dA'}&=\frac{1}{r'}\,\frac{d(\cos\Theta)}{dr'}\,\frac{d\Phi}{d\Phi'}\\ &=\frac{1}{r'}\,\frac{eV}{2\varepsilon D}\sin\Theta\left(\cos\Theta-\sqrt{\cos^2\Theta+\frac{eVd}{\varepsilon D}}\right)^{-1}\\ &\quad\times\left(\cos\Theta+\frac{\sin^2\Theta}{\sqrt{\cos^2\Theta+eVd/\varepsilon D}}\right)^{-1}. \end{aligned} \tag{A6}$$

The azimuthal angle in the image plane, Φ', is identical to the azimuthal angle of the photoelectron momentum in the atomic frame, Φ, so $d\Phi/d\Phi'=1$. Combining Eqs. (8), (A5), and (A6), we can calculate an image of the photoelectrons on the phosphor screen of our detector for any polarization of the laser, given the radial transition moments and continuum phase differences. We use these calculated images for direct comparison with measured images in Sec. V.

We can also determine the radius of the image in the plane of the phosphor screen using Eq. (A6). At this maximum radius, the density function $d\Omega/dA'$ tends to ∞, yielding

$$r'_{\max}=\frac{2\varepsilon D\sqrt{1+eVd/\varepsilon D}}{eV}. \tag{A7}$$

The factor $\int_V dV\int_t dt F^2(\vec{r},t)\rho_{at}$ that appears in Eq. (A5) is difficult to determine with high precision, but is relatively constant over the duration of our measurements. Its determination is not necessary in measurements of $d\sigma/d\Omega$, as it affects only the overall magnitude of our signal. We do not consider this factor further in this work.

[1] J.A. Duncanson, Jr., M.P. Strand, A. Lindgård, and R.S. Berry, Phys. Rev. Lett. **37**, 987 (1976); J.C. Hansen, J.A. Duncanson, Jr., R.-L. Chien, and R.S. Berry, Phys. Rev. A **21**, 222 (1980).

[2] A. Siegel, J. Ganz, W. Bußert, and H. Hotop, J. Phys. B **16**, 2945 (1983).

[3] H. Kaminski, J. Kessler, and K.J. Kollath, Phys. Rev. Lett. **45**, 1161 (1980).

[4] U. Heinzmann, J. Phys. B **13**, 4353 (1980); Ch. Heckenkamp, F. Schäfers, G. Schönhense, and U. Heinzmann, Phys. Rev. Lett. **52**, 421 (1984); Z. Phys. D: At., Mol. Clusters **2**, 257 (1986).

[5] A. Hausmann, B. Kämmerling, H. Kossmann, and V. Schmidt, Phys. Rev. Lett. **61**, 2669 (1988).

[6] K.L. Reid, D.J. Leahy, and R.N. Zare, Phys. Rev. Lett. **68**, 3527 (1992).

[7] C.S. Feigerle, R.N. Compton, L.E. Cuéllar, N.A. Cherepkov, and L.V. Chernysheva, Phys. Rev. A **53**, 4183 (1996).

[8] Yi-Yian Yin and D.S. Elliott, Phys. Rev. A **47**, 2881 (1993).

[9] A. Burgess and M.J. Seaton, Mon. Not. R. Astron. Soc. **120**, 121 (1960).

[10] G. Peach, Mem. R. Astron. Soc. **71**, 13 (1967).

[11] F. Arqueros, P.E. LaRocque, M.S. O'Sullivan, and B.P. Stoicheff, Opt. Lett. **9**, 82 (1984).

[12] B.P. Stoicheff and E. Weinberger, Can. J. Phys. **57**, 2143 (1979).

[13] S.A. Lee, J. Helmcke, J.L. Hall, and B.P. Stoicheff, Opt. Lett. **3**, 141 (1978).

[14] C.J. Sansonetti and K.-H. Weber, J. Opt. Soc. Am. B **2**, 1385 (1985).

[15] Zheng-Min Wang and D.S. Elliott, Phys. Rev. Lett. **84**, 3795 (2000).

[16] H.B. Bebb and A. Gold, Phys. Rev. **143**, 1 (1966).

[17] P. Lambropoulos and M.R. Teague, J. Phys. B **9**, 587 (1976).

[18] M. Born and E. Wolf, *Principles of Optics*, 6th ed. (Permagon Press, Oxford, 1980).

[19] M.P. Strand, J. Hansen, R.L. Chien, and R.S. Berry, Chem. Phys. Lett. **59**, 205 (1978).

[20] G. Leuchs, S.J. Smith, E. Khawaja, and H. Walther, Opt. Commun. **31**, 313 (1979).

[21] G. Leuchs and H. Walther, in *Multiphoton Ionization of Atoms*, edited by S.L. Chin and P. Lambropoulos (Academic, Toronto, 1984).

[22] H. Helm, N. Bjerre, M.J. Dyer, D.L. Huestis, and M. Saeed, Phys. Rev. Lett. **70**, 3221 (1993).

[23] M.G. Littman, Appl. Opt. **23**, 4465 (1984).

[24] Yi-Yian Yin, Ce Chen, D.S. Elliott, and A.V. Smith, Phys. Rev. Lett. **69**, 2353 (1992).

[25] X. Tang and P. Lambropoulos, as reported by A. Dodhy, R. N. Compton, and J. A. D. Stockdale, Phys. Rev. Lett. **54**, 422 (1985).

[26] M.S. Pindzola, as reported by A. Dodhy, R. N. Compton, and J. A. D. Stockdale, Phys. Rev. Lett. **54**, 422 (1985).

[27] H.A. Bethe and E.E. Salpeter, *Quantum Mechanics of One- and Two-Electron Atoms* (Plenum, New York, 1977).

[28] E. Fermi, Z. Phys. **59**, 680 (1930).

[29] E. Caliebe and K. Niemax, J. Phys. B **12**, L45 (1979).

[30] D. von der Goltz, W. Hansen, and J. Richter, Phys. Scr. **30**, 244 (1984).

[31] W. Hansen, J. Phys. B **17**, 4833 (1984).